

Oxide Film Growth by CSV on AISI 316L: a Combined Electrochemical and Analytical Characterization

Belén Díaz,^a Lorena Freire,^{*,a,b} Maria Fátima Montemor^b and Xosé Ramón Nóvoa^a

^aGrupo de Enxeñaría de Corrosión e Materiais (ENCOMAT), Escuela de Ingeniería Industrial, Universidade de Vigo, Campus Universitario, 36310 Vigo, Spain

^bInstituto de Ciências e Engenharia de Materiais e Superfície (ICEMS), Instituto Superior Técnico, Universidade Técnica de Lisboa, Av. Rovisco Pais, 1049-001 Lisbon, Portugal

A composição dos filmes de óxidos formados em aço inoxidável é fundamental no comportamento da corrosão destes materiais. Suas características têm sido largamente estudadas, mas ainda geram muitas questões, especialmente com relação aos mecanismos de crescimento do óxido e alterações em sua composição durante o crescimento do filme. Este trabalho visou estudar a composição química e o comportamento electroquímico destes filmes formados em condições distintas em substratos de AISI 316L. Investigou-se o efeito do número de ciclos, velocidade de varredura de potencial, composição do electrólito e pH na resposta eletroquímica dos óxidos formados. O aumento da velocidade de varredura promoveu a formação de filmes mais finos, de menor condutividade e mais ricos em Fe³⁺, principalmente hidróxidos. O estudo revelou uma dependência da composição do filme com o valor de pH, filmes formados em meios neutros apresentaram mais elevada resistividade e maior conteúdo de espécies de Fe e traços de Mo comparativamente a filmes formados em meio alcalino.

The composition of the oxide layers formed in stainless steels is fundamental in the corrosion behavior of these materials. Its characterization has been widely studied, but still many questions arise, especially mechanisms of oxide growth and changes in its composition during the film development. This work aimed to study the chemical composition and electrochemical behavior of these films formed in different conditions of substrates de AISI 316L. The work investigated the effect of the number of cycles, scan rate, electrolyte composition and pH in the electrochemical response of the formed oxides. The increase of the scan rate promoted the formation of thinner films, richer in Fe³⁺ species, mainly hydroxide, with decreased conductivity. The study revealed a pH-dependent film composition, films formed in near neutral solutions presented higher resistivity and higher content of Fe species and traces of Mo compared to films formed in alkaline medium.

Keywords: cyclic sweep voltammetry (CSV), impedance (EIS), oxide film, stainless steel

Introduction

Stainless steels find many applications in which corrosion resistance is a mandatory requirement. These materials are stable in a wide range of conditions and media due to the formation of Cr-rich stable passive films. The study of the properties of the passive films formed on stainless steels has been widely studied and reviewed by Olsson and Landolt.¹ Relevant parameters such as thickness or composition have been investigated as a function of the electrolyte composition, the pH or the alloying elements.¹

Surface analytical techniques such as X-ray photoelectron spectroscopy (XPS), Auger electron spectroscopy (AES) or scanning tunnelling microscopy (STM) have been widely employed for the film characterization.

On the other hand, electrochemical methods provide a simple procedure to characterize material surfaces, allowing its accurate characterization. In particular, cyclic sweep voltammetry (CSV) is a well-known electrochemical procedure used to grow surface films, while acquiring information on the redox behavior of electrochemically active species, on the kinetics of electrode reactions and on the presence of electroactive species either in solution or at the electrode surface.^{2,3}

*e-mail: lorenafp@uvigo.es

Recently, stainless steels have attracted much attention as current collectors or electrodes in systems for energy storage such as batteries, solid oxide fuel cells and supercapacitors because of the lifetime and competitive prices. In such applications, oxide layers of various thicknesses can be formed and different oxide film properties must be thought depending on the function. For example, in solid oxide fuel cell (SOFC) interconnects, thick, stable and non-resistive films should be formed in order to allow the desired conductivity and avoid Cr poisoning. In supercapacitors, the surface films must be highly conductive to avoid loss of efficiency and decreased cycleability. Moreover, in these applications, the steel materials can be exposed to very different environments, such as very alkaline, neutral or very acidic, as well as exposed to sudden potential variations. Films can be formed by various electrochemical techniques such as anodic polarization, cyclic sweep voltammetry and electrodeposition (either anodic or cathodic). Therefore, nowadays there is a renewed interest on the electrochemical growth of oxide films formed on stainless steels and its characterization targeting applications in energy storage/production devices. Thus, the present work aims at contributing for a deeper characterization of thicker oxide films grown on AISI 316L stainless steel, a material that is now finding many applications in the energy storage domain.¹

Concerning the state-of-art, there have been numerous studies on the electrochemical characterization of passive films formed on steels in different environments.⁴⁻¹¹ However, only few of them are concerned with the characterization of thick films formed by CSV,^{6,12-15} using electrochemical techniques such as impedance spectroscopy (EIS).^{7,12,13,16} Indeed, systematic studies comparing the properties of the surface films formed by CSV in different electrolytes from neutral to alkaline conditions are needed to point out the main differences and similarities between these films. Besides the electrolyte composition, the number of cycles and the scan rate are parameters affecting the properties of the oxide films generated by CSV.^{11,13}

The present work aims at contributing for a better understanding of the electrochemical behavior of AISI 316L stainless steel oxides potentiodynamically generated in different electrolytes typically found in some energy devices (KOH and Na₂SO₄).¹⁷⁻²⁰ For instance, in such studies it was observed that the lowest capacitance of magnetite in KOH could be attributed to the slow formation

of an insulating layer on the magnetite surface, which may affect the performance of these materials in energy storage and production devices.

In this work, oxide films were formed by CSV. During oxide formation, the current can be monitored continuously and the oxide growth is followed during the whole experiment, a great advantage over other oxide development procedures.^{3,21} In order to produce oxides with different thicknesses, compositions and electrical properties, the effect of variables such as electrolyte composition (Cl⁻ and SO₄²⁻), pH (13 and 7) and polarization rate (2, 5 and 10 mV s⁻¹) were studied.

The electrochemical characterization of the formed oxide films was completed by using EIS spectroscopy. This study was combined with surface analysis by XPS spectroscopy.

Experimental

Passive oxide film growth and electrochemical analysis

The chemical composition (wt.%) of AISI 316L stainless steel employed in this study is depicted in Table 1. The samples were abraded with wet emery paper of decreasing grit size down to 4000, and then polished with alumina paste (1 μm) to get a mirror-like surface. After polishing, the samples were degreased with acetone and rinsed ultrasonically in distilled water. Then, the samples were dried in a dry air stream and kept in a desiccator prior to cycling.

The passive oxide films were grown in three different electrolytes, one alkaline and two near neutral. The alkaline solution (0.1 mol L⁻¹ NaOH) was prepared with and without the addition of chloride ions (added as NaCl to reach 0.1 mol L⁻¹ concentration). The two neutral solutions were 0.1 mol L⁻¹ Na₂SO₄ (pH 7) and 0.1 mol L⁻¹ NaCl (pH 7). The solutions were prepared with p.a. chemicals and deionized water.

The passive layers were electrochemically generated using an Autolab PGSTAT 30 from Ecochemie®. A conventional three-electrode electrochemical cell, placed inside a Faraday cage, was employed. Different reference electrodes were used depending on the electrolyte in order to avoid any kind of contamination.²² The Hg/HgO (1 mol L⁻¹ KOH) electrode was employed for the alkaline electrolyte, the Hg/Hg₂SO₄ (K₂SO₄ saturated) electrode was employed for the sulfate electrolyte, and the saturated calomel

Table 1. Chemical composition of the stainless steel AISI 316 used in this study

	C	P	S	Si	Mn	Cr	Ni	Mo	Cu	Ti	N	Fe
Composition / wt.%	0.031	0.02	0.001	0.45	1.66	16.85	11.75	2.10	0.31	0.211	0.024	balanced

electrode (SCE) Hg/Hg₂Cl₂ (KCl saturated) was employed for the chloride containing solution. All the potentials in the text are referred to the SCE. A platinum mesh was used as a large area counter electrode. The working electrode area was 0.34 cm². All the electrochemical tests were performed at room temperature and under aerated conditions.

CSV technique was used to grow the oxide layers. The potentiodynamic curves were obtained by polarizing the working electrode in the potential window of water stability. Three different scan rates were selected for the film grown (2, 5 and 10 mV s⁻¹) to study the effect of the scan conditions on the oxide properties. The effect of the scan rate was studied in alkaline solution, 0.1 mol L⁻¹ NaOH. In order to check the effect of the pH and the electrolyte composition, films formed at a scan rate of 5 mV s⁻¹ in 0.1 mol L⁻¹ NaOH + 0.1 mol L⁻¹ NaCl and in neutral solutions containing Cl⁻ or SO₄²⁻ were investigated as well. The polarization procedure was repeated up to 20 cycles, until stable current densities were obtained.

EIS measurements were carried out before and after the film formation. The spectra were obtained at the open circuit potential (OCP), applying a sinusoidal potential oscillation of 10 mV rms (root mean square) amplitude. The frequency was swept from 10 kHz down to 1 mHz, with seven points *per* decade.

Surface characterization

XPS measurements were performed using a Microlab 310 F (Thermo Electron, former VG Scientific) equipped with a Mg (non-monochromated) anode and a concentric hemispherical analyzer. The XPS analysis was performed under pressures below 5 × 10⁻⁹ mbar, using an Al radiation (non-monochromated). The spectra were taken in CAE (constant analyzer energy) mode (30 eV) and accelerating voltage of 15 kV. The peak quantification was determined after fitting. The fitting function used was a Gaussian-Lorentzian product function and the algorithm was based on the Simplex optimization as used in the Advantage[®] software.

A JEOL JSM-5410 scanning electron microscope (SEM) was employed to study the structure and morphology of the electrochemically generated films.

Results and Discussion

Effect of the scan rate

Cyclic voltammetry analysis

Figure 1a depicts the evolution of the potentiodynamic polarization curves registered for the films formed at

the slowest scan rate, 2 mV s⁻¹, in 0.1 mol L⁻¹ NaOH. Three different regions in the voltammograms can be differentiated. The assignment of the different peaks has been reported in previous publications.^{23,24} The first region, for potentials lower than -600 mV, corresponds to the iron activity. The main feature in this potential range is associated with the magnetite formation peak, Fe₃O₄,

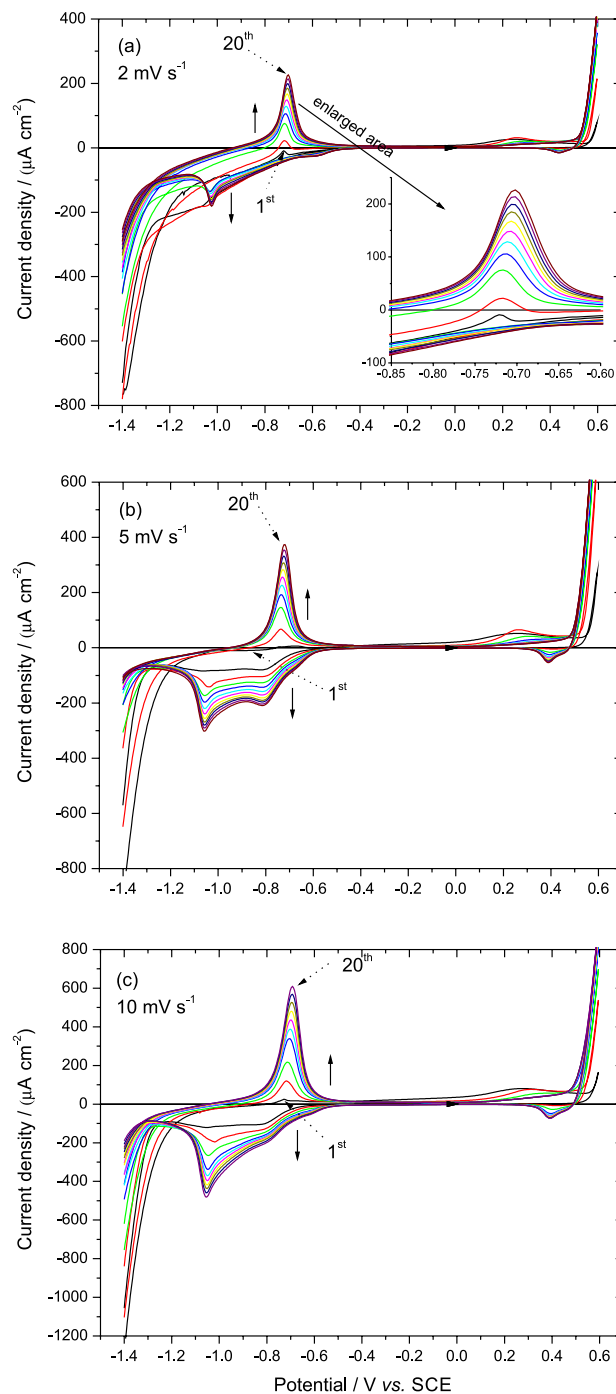
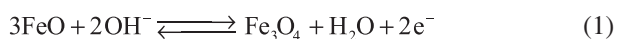


Figure 1. Cyclic voltammetry curves (from 1st to 20th cycle) for the AISI 316L obtained in 0.1 mol L⁻¹ NaOH, at: (a) 2 mV s⁻¹, the anodic peak for the magnetite formation is presented in the enlarged area, (b) 5 and (c) 10 mV s⁻¹ scan rates.

at approximately -700 mV. The passivity range extends from -600 to $+200$ mV, being characterized by very low current density values. Finally, at more anodic potentials, the redox processes associated with low-high oxidation states of Cr, Ni and Mo are detected ($\text{Cr}^{3+}/\text{Cr}^{6+}$, $\text{Ni}^{2+}/\text{Ni}^{3+}$ and $\text{Mo}^{4+}/\text{Mo}^{6+}$). During the cycling process, the original thin native oxide film, mainly composed of Cr and Fe oxides,²⁵ is converted into a thicker and more conducting layer, mainly based on magnetite.²⁶ The magnetite development, at about -700 mV, follows the redox reaction described in equation 1.



The current involved in the magnetite formation peak increases during the potentiodynamic cycling, as expected, suggesting oxide growth. During the potentiodynamic cycling, the potential characteristic of magnetite shifts to nobler values, increasing from -720 to -700 mV, as graphically detailed in Figure 1a, and numerically shown in Figure 2a. Such behavior was already reported in the

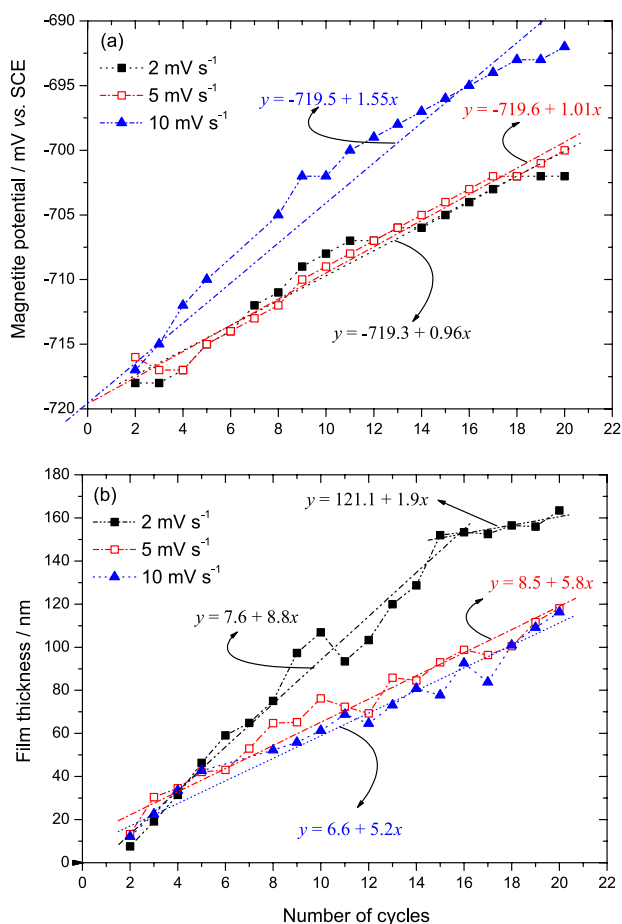


Figure 2. Evolution with the number of cycles in 0.1 mol L⁻¹ NaOH solution of (a) the characteristic potential of the magnetite formation peak and (b) the magnetite film thickness.

literature,¹¹ and is related to a progressive enrichment of the oxide film in Fe³⁺ species in the outer part of the oxide film. This change is usually associated with an increase of the ohmic drop in the layer as reported.^{16,27}

At the anodic limit of the voltammogram, the oxygen evolution (ca. $+0.5$ V) is displaced to lower potential values as cycling proceeds, showing a kind of activation for the O₂ evolution process with the progress in the oxide layer chemical state in agreement with previous literature.²⁸

The magnetite oxidation process is negligible (very small anodic peak at the beginning of the passive region). Moreover, as magnetite is reduced in the cathodic cycle to a large extent, the thickness of the magnetite rich layer at cycle i can be estimated from the corresponding charge involved in the magnetite formation peak, Q_i in equation 2. The area corresponding to the peak was first calculated and the corresponding thickness determined using Faraday's law (equation 2). The values assumed in this equation are: Fe₃O₄ molecular weight (M) 231.5 g mol⁻¹ and its density (ρ) 5.2 g cm⁻³.²⁹ Then, the magnetite thickness (d_i) at cycle i , which is proportional to the passive oxide thickness, was calculated as a function of the cycle number as indicated in Figure 2b. The film formation follows a quite well defined linear tendency, obtaining for these experimental conditions a rate of oxide growth of 8.8 nm *per cycle*. By the cycle 15, the rate of film growth decreased to 1.9 nm *per cycle*, which corresponds to the near steady voltammogram situation. This variation will be discussed in the next paragraphs. The estimated film thicknesses are in the same order of magnitude of layers grown in similar conditions on identical substrates and measured by XPS depth profiling and reported elsewhere.³⁰ The coincidence between the electrochemical estimation of thickness assuming magnetite as the only passivating species and the XPS depth profiling can be understood supposing that the dominant species in the electrochemically grown film are iron oxides.³¹ The reason for this is twofold: Cr³⁺ is oxidized at the anodic limit of the potential window giving soluble chromates, and Ni²⁺ leaves the oxide structure and accumulates as metallic nickel at the metal-oxide interface.

$$m_i = \frac{M}{zF} Q_i = \frac{M}{zF} \int_{-0.84V}^{-0.60V} I_i dt \quad d_i = \frac{m_i}{\rho} \quad (2)$$

m_i is the mass formed on the metal surface at cycle i ; F is Faraday constant (96500 C equivalent⁻¹); z is the number of electrons involved in the reaction process depicted in equation 1 (equivalent mol⁻¹).

Passive oxide layers were also grown at 5 and 10 mV s⁻¹ in the same alkaline electrolyte. The corresponding

voltammetric curves are presented in Figures 1b and 1c. The magnetite formation peak at about -700 mV is also well defined and, as for the 2 mV s^{-1} sweep rate, the oxide layer growth is confirmed by the current increment with cycling. The characteristic potential of the magnetite formation peak shifts in the nobler direction, as indicated in Figure 2a. The rate of the anodic shift with cycling increases with the sweep rate (see slopes of the apparent linear fittings also depicted in Figure 2a). Therefore, this study allows to conclude that the oxide films grown by CSV oxidize faster when formed at higher scan rates.

The thickness of the passive film was also estimated using equation 2 as shown in Figure 2b. Lower slopes were obtained at faster sweep rates in comparison to the slower scan rate (2 mV s^{-1}), as indicated in the corresponding linear fits, confirming a decreased oxide growth rate probably due to its more resistive character. However, no significant differences between the cycling at 5 and 10 mV s^{-1} could be observed. It seems that an asymptotic growth rate was reached at 5 mV s^{-1} .

It is worth mentioning the ordinate values obtained in the fittings for the three scan rates at $x = 0$ in Figure 2b. Those values (6.6, 7.6 and 8.5 nm) should correspond to the native oxide thickness, and are in the same order of magnitude measured by XPS depth profiling.²¹

As mentioned before, Figure 2b shows that the film thickness tends to an asymptotic value around the 15th cycle for the slowest scan rate, which was not observed for the 5 or 10 mV s^{-1} cycling rates. Thus, the film growth seems to become more difficult after the 15th cycle for the 2 mV s^{-1} cycling rate.

After the 15th cycle, the film grows at approximately 1.9 nm per cycle , five times less than the rate measured before the 15th cycle (8.8 nm per cycle). This reduction agrees with the stabilization trends observed in Figure 2a, concerning the behavior of the characteristic potential of the magnetite formation peak. Thus, it can be said that the rate of film growth slows down when the oxidation to Fe^{3+} species in the outer part of the passive film is completed, which involves a change in the growth mechanism. The critical thickness at which that change occurs should be close to 121 nm , as indicated from the apparent linear fitting ordinate value depicted in Figure 2b.

For the faster scan rates, the decreased development (critical film thickness) was not reached in the conditions of the experiment.

The time consumed for the oxide growth is obviously shorter for the same number of scans when cycling at a faster rate. However, taking into account the linear fits presented in Figure 2b, a thicker film could be developed cycling faster (5 or 10 mV s^{-1}) if the cyclic sweep is run

for an equivalent time. For 10 mV s^{-1} , the oxide film growth is 5.2 nm per cycle (from the linear fitting) in such a way that to get an equivalent film to that growth at 2 mV s^{-1} (ca. 160 nm), the sweep should be run up to 30 cycles, but considerably reducing the total treatment time. However, it must be stressed that the oxides grown at the different rates show different properties as discussed below. On the other hand, the stabilization in the growth process seems to arise after a certain number of scans as well.

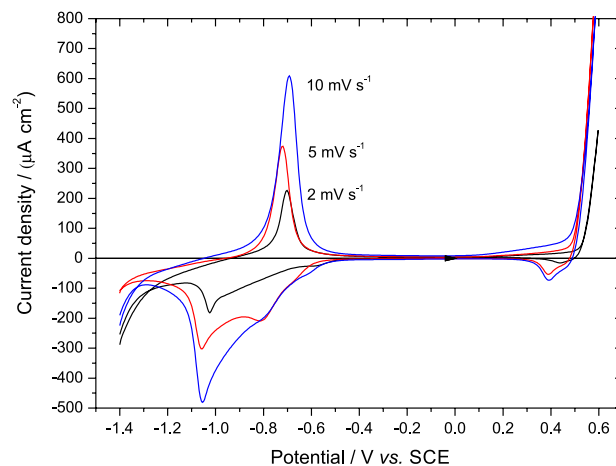


Figure 3. Polarization curves obtained in 0.1 mol L^{-1} NaOH at 2, 5 and 10 mV s^{-1} . The 20th cycle is compared.

The cyclic voltammetric curves obtained after the 20th cycle in 0.1 mol L^{-1} NaOH at 2, 5 and 10 mV s^{-1} scan rates are compared in Figure 3. The characteristic peaks are very similar in the three voltammograms, with an apparent peak current density proportional to the scan rate. When the scan rate increases, there is a linear increase of the current density in both anodic and cathodic curves, according to equation 3. The Faradaic current (I_F) associated with the electron transfer resulting from oxidation/reduction of electroactive species is increased by the capacitive charging current (I_C). The total current is then defined as indicated in equation 3. The peak intensity is proportional to the scan rate (dE/dt).³² However, in the present case, taking $C = 50 \text{ µF cm}^{-2}$, the maximum expected I_C (for 10 mV s^{-1} scan rate) is 0.5 µA cm^{-2} , i.e., less than 0.5% of the recorded currents in Figure 3. Thus, in equation 3, $I \cong I_F$, which means that the differences observed in the peak currents correspond to the different degrees of development of the passive film at this particular cycle, in accordance with the above discussion for Figure 2b. This result also validates the calculations made from equation 2, where the capacitive current was neglected.

$$I = I_F + I_C = I_F + C \frac{dE}{dt} \quad (3)$$

Electrochemical impedance spectroscopy analysis

EIS was also used for the characterization of the oxide films formed by voltammetry. Figure 4 shows a comparison between the Bode plots obtained before and after the potentiodynamic cycling at the three scan rates studied in alkaline media. For the three experiments, a change was observed in the phase angle plot that allows

to better differentiate between, the presence of two time constants. This effect is more evident for the lower scan rate (Figure 4a). Figure 4a shows that the low frequency limit of the impedance modulus decreases after cycling.

Nevertheless, at 5 and 10 mV s^{-1} (Figures 4b and 4c, respectively), an opposite trend was observed. Assuming that the low frequency process is related to the passive film properties, this trend suggests changes on the film conductivity, in agreement with the previous results. The results suggest that at lower scan rates, the film is more conductive, whereas at increased scan rate, a more resistive film seems to be produced. To obtain more detailed information on the electrochemical processes associated with the oxide films formed at different conditions, the impedance spectra were analyzed using the equivalent circuit presented in Figure 4d.

Although there are other possible equivalent circuits, which would easily fit the experimental data, the one adopted for this study consists of two time constants distributed hierarchically. The equivalent circuit, according to the impedance function given in equation 4, has been reported as suitable to model the behavior of stainless steels in different media.^{30,33} One possible interpretation for the circuit elements in this circuit is as follows: R_e is associated with the electrolyte resistance, the high frequencies time constant (R_1C_1) is associated with the charge transfer resistance (R_1) in parallel with the double layer capacitance (C_1). The low frequency time constant (R_2C_2) has been proposed to describe the redox processes taking place in the oxide film (see next for details). The parameters α_1 and α_2 model the Cole-Cole type dispersion of the time constants.³⁴

The best fitting parameters are reported in Table 2. For the exponents, α_1 and α_2 have values close to 0.9 in all cases.

$$Z(\omega) = R_e + \frac{R_1}{(j\omega R_1 C_1)^{\alpha_1} + 1 / (1 + (Z_2(\omega) / R_1))} \quad (4)$$

$$Z_2(\omega) = \frac{R_2}{1 + (j\omega R_2 C_2)^{\alpha_2}}$$

For the three samples, R_1 decreases after cycling, probably due to chromite dissolution and magnetite enrichment in the surface film as suggested elsewhere.³⁰ As the scan rate increases, the differences between the R_1 values obtained before and after the cycling, attenuate. R_1 reduces by 85, 74 and 35% in comparison with the values before cycling for 2, 5 and 10 mV s^{-1} , respectively. The reduction of the charge transfer resistance value agrees with the development of an oxide film with higher conductivity, which contains a lower proportion of Cr_2O_3 , which is one of the species contributing for the resistive

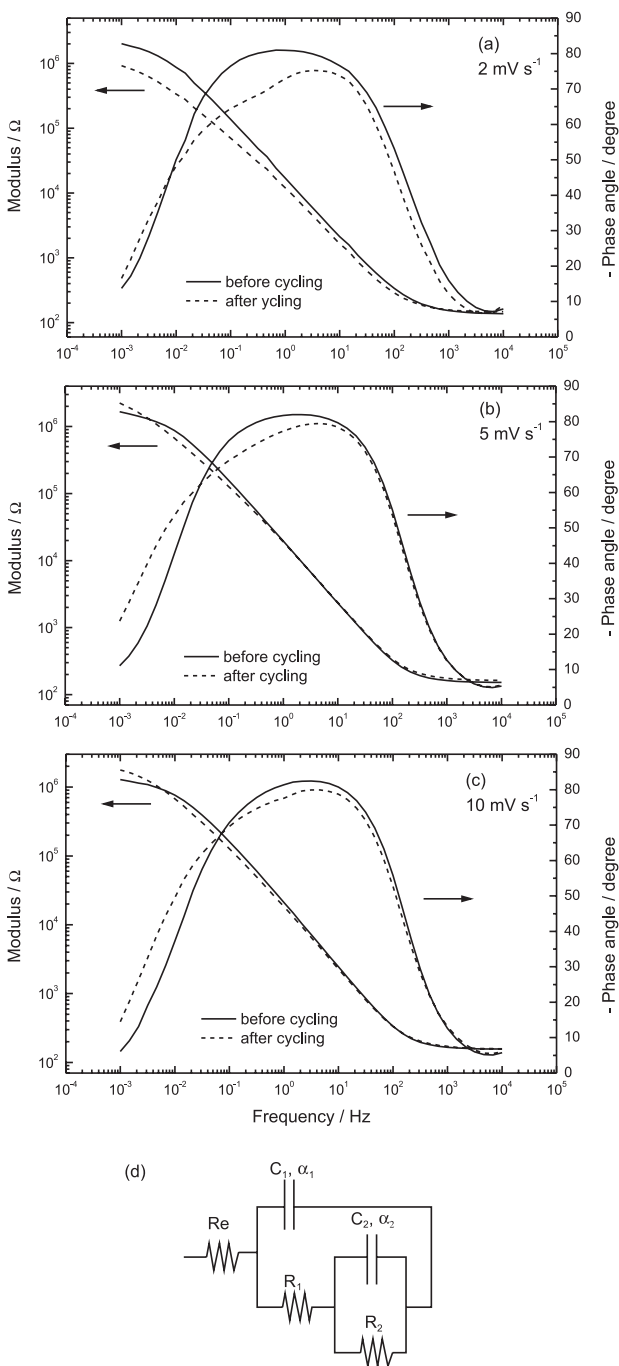


Figure 4. Bode plots measured before and after cycling in 0.1 mol L^{-1} NaOH at (a) 2, (b) 5 and (c) 10 mV s^{-1} scan rates and (d) the equivalent circuit followed for the impedance fitting.

Table 2. Best fitting parameters obtained following the equivalent circuit proposed in Figure 4d, before and after the immersion in the specified conditions

	OCP / mV	R _e / (Ω cm ²)	R ₁ / (kΩ cm ²)	C ₁ / (μF cm ²)	R ₂ / (kΩ cm ²)	C ₂ / (μF cm ²)
0.1 mol L ⁻¹ NaOH 2 mV s ⁻¹	before					
	-332	48.1	295.1	41.5	578.0	2.9
	after					
	-417	50.2	44.9	53.8	30.2	73.2
0.1 mol L ⁻¹ NaOH 5 mV s ⁻¹	before					
	-398	52.2	311.5	32.5	198.3	31.8
	after					
	-418	56.2	79.7	30.3	850.0	48.1
0.1 mol L ⁻¹ NaOH 10 mV s ⁻¹	before					
	-383	53.7	171.8	27.6	239.3	27.4
	after					
	-393	54.6	111.2	33.2	510.0	34.1
0.1 mol L ⁻¹ NaCl 5 mV s ⁻¹	before					
	-231	142.8	166.6	69.4	34.9	325.6
	after					
	-245	121.8	325.4	95.3	2006.0	442.9
0.1 mol L ⁻¹ Na ₂ SO ₄ 5 mV s ⁻¹	before					
	-162	70.6	137.7	41.8	218.6	127.6
	after					
	-66	78.7	414.8	144.7	21930.0	699.7

behavior of the oxide film. For the faster cycling rate, a lower amount of magnetite is potentiodynamically generated and, in consequence, a higher percentage of the native Cr₂O₃ is still present after the polarization. This different oxide composition is responsible for the poorer oxide conductivity measured under these conditions. These results are in good agreement with the larger thickness found for the magnetite at slower sweep rates as discussed in the previous section.

Table 2 also shows that the R₂ value decreases after cycling at 2 mV s⁻¹. However, it shows an increase for the higher scan rates. R₂ can be assigned to changes in the oxide film, and it has been attributed to the magnetite transformation rate to Fe³⁺, as indicated in equation 5.³⁴ Therefore, it is possible to distinguish two types of films from the results obtained by fitting the EIS spectra:²⁶ films grown at the slower scan rate (2 mV s⁻¹), where the redox process is relatively fast, and the two other cases, where that process is slower.



The capacitance values evidence also some differences as a function of the scan rate. The capacitance that is assumed to be associated with the double layer (C₁) does

not change significantly, although there is a slight increase for the slower scan rate. Since this capacitance is directly related to the active electrode surface, the increase in the C₁ can be associated with an increase of the active surface and/or higher surface roughness as a consequence of the potentiodynamically developed oxide layer.

The effects on C₂ are again more evidenced for the slower scan rate. C₂ can be evaluated from equation 6, where q is the total charge stored in the passive film and θ is the transformation degree of the oxide film at a given potential (E).³⁵

$$C_2 = q \frac{\partial \theta}{\partial E} \quad (6)$$

As the potential values registered before and after the polarization are very similar in the three cases, as indicated in Table 2, the capacitance C₂ can be related to the available magnetite charge, and therefore to the magnetite layer thickness. Consequently, after cycling at 2 mV s⁻¹, a thicker film of magnetite is formed, in agreement with the higher values of effective charge registered after polarizing at this scan rate. The percentage of increment for the C₂ is decreased after cycling at 5 mV s⁻¹ and it is even lower for the 10 mV s⁻¹ scan rate.

An interesting aspect to be noticed in Table 2 concerns the initial C_2 capacitance values that are not equal for the different (nominally identical) samples. However, a correlation exists between the OCP values and the C_2 values: higher C_2 values correspond to more cathodic OCP values. That relationship has already been observed^{36,37} and is directly related to the parameter q in equation 6. At more anodic potential values, only the redox process depicted in equation 5 is active (magnetite oxidation/reduction), while for more cathodic potential values, the backward process of the redox reaction depicted in equation 1 (magnetite formation/reduction) starts to become important, thus contributing to the total charge q in equation 6. The conclusion is that, although nominally identical, the starting oxide films present dissimilar degree of oxidation (Fe^{3+}/Fe^{2+} ratio).³⁸ Those differences are, however, not relevant in the study because no cross-comparisons are performed.

Surface analysis

The SEM pictures taken after the cycling are presented in Figure 5. The film morphology depends upon the scan rate. The morphology is more uniform for the films formed at 2 and 5 $mV s^{-1}$ scan rate, whereas increasing the sweep rate leads to an uneven film morphology or topotactic development.³⁹ These observations correlate well with the results discussed from the electrochemical data. Higher surface roughness is confirmed for the oxides formed at lower scan rate, in agreement with the increased double layer capacitance (C_1). The non-uniform growth at faster sweep rates suggests a lower extent in the processes of dissolution of chromite and development of the magnetite layer.

In order to detail the chemical composition of the oxide films obtained, XPS analysis was performed as well. The Fe 2p, Cr 2p and O 1s high resolution ionizations are presented in Figure 6. The O 1s ionization shown in Figure 6c is composed of three peaks for the three different oxides studied. The main peak, centered at about 532.4 ± 0.3 eV, shows the presence of hydroxides, probably Fe-hydroxides as well as adsorbed hydroxyl groups on the surface.⁴⁰ The peak at the lowest binding energy (530.3 ± 0.3 eV) corresponds to the presence of oxide species. The peak detected at the highest binding energy (534.7 ± 0.3 eV) for this study is typically attributed to adsorption of water molecules. The atomic percentage for the main signal related to the OH^- containing species increases for the faster scans from 64% (at 2 $mV s^{-1}$) to 81% (at 5 and 10 $mV s^{-1}$). The signal associated with the oxide anions decreases from 29 to 11%, whereas that for the adsorbed water remains almost constant. Thus, a surface film with a lower fraction of hydroxide⁴¹ and probably more

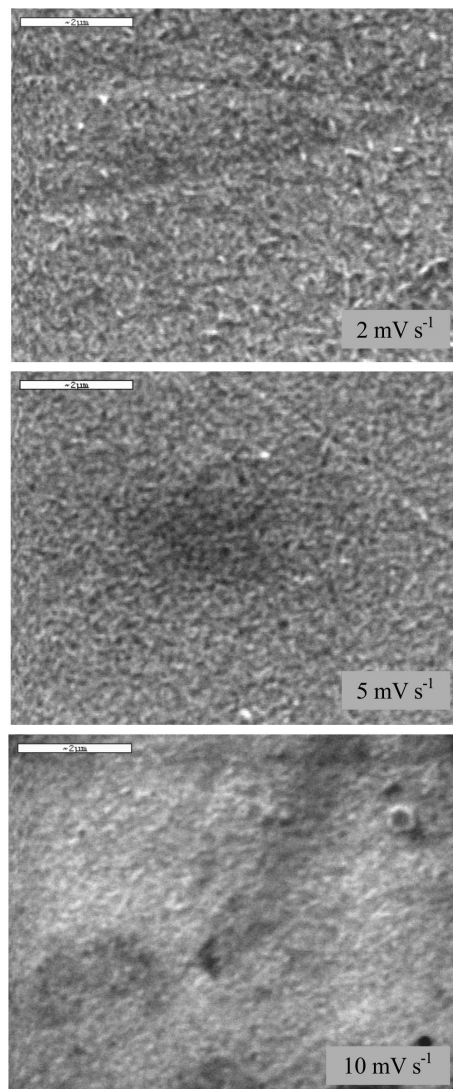


Figure 5. SEM images obtained after cycling in 0.1 mol L⁻¹ NaOH at 2, 5 and 10 $mV s^{-1}$, magnification of 15000 \times .

conductive character develops at the lowest scan rate.

The presence of metallic Fe is excluded since no signal below 707 eV⁴² could be detected (Figure 6a). In the Fe 2p₃ ionization, four different contributions could be deconvoluted for the oxide films formed at 2 and 5 $mV s^{-1}$. One of these peaks is located in the low binding energy side 708.1 ± 0.4 eV. At the highest scan rate (10 $mV s^{-1}$), this peak is not observed. This peak shows a binding energy lower than that typically expected for Fe^{2+} , which is around 709 eV,⁴³ but it can be associated with Fe^{2+} . In fact, the literature reports the presence of Fe^{2+} in the range 708.0 - 708.5 eV.^{44,45} Another interpretation proposed in the literature is that the presence of a peak at 707.9 eV can be due to the presence of metallic iron strongly interacting with the oxide.⁴⁶ These species are not detected at the highest scan rate in agreement with the faster oxidation under these conditions as previously discussed.

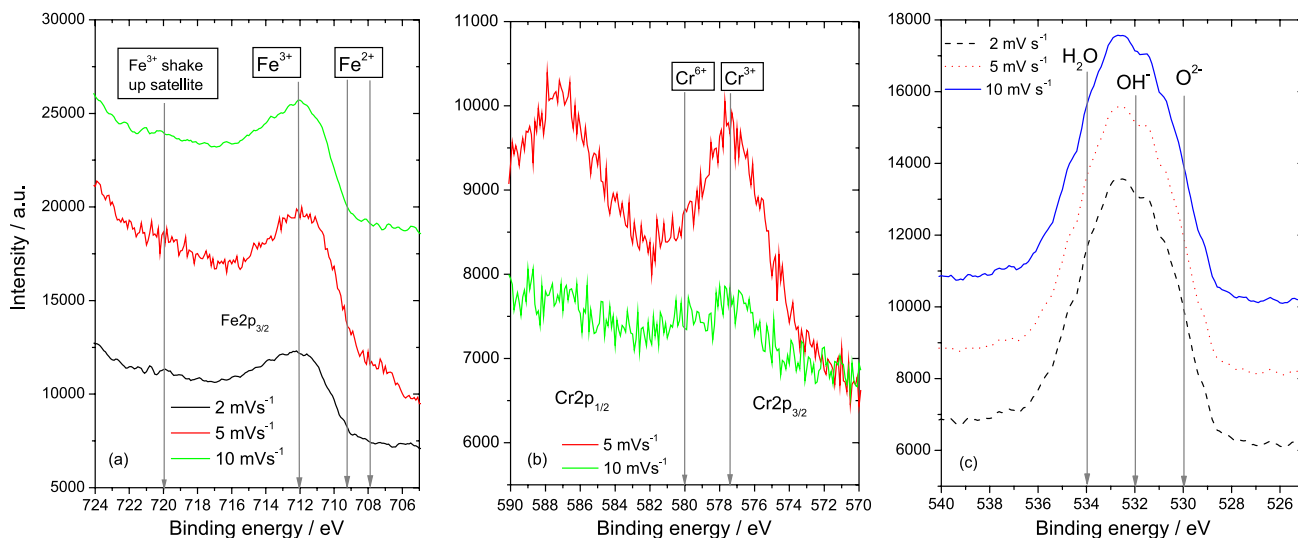


Figure 6. XPS spectra of the (a) Fe 2p, (b) Cr 2p and (c) O 1s ionizations for the films formed in 0.1 mol L⁻¹ NaOH at 2, 5 and 10 mV s⁻¹ scan rates. No signal was detected for the Cr 2p at the slowest scan rate.

Other three different peaks were identified in the Fe 2p_{3/2} ionization. The peak at 710.3 eV can be attributed to Fe²⁺ or Fe³⁺ species in the form of oxides. Considering that the presence of magnetite can be observed in this range,⁴⁷ overlapping with Fe²⁺ oxide/hydroxide, thus the deconvolution of the magnetite peak is not accurate due to this superimposition of species. At 711.8 ± 0.4 and 713.2 ± 0.1 eV, the signals related to Fe³⁺ ions from Fe₂O₃/FeOOH or hydrated species are detected, in agreement with literature. Some authors have related this higher binding energy signals to the sum of multiplet peaks, attributing the highest energy one to α-Fe₂O₃^{48,49} and/or γ-Fe₂O₃, γ-FeOOH and α-FeOOH.⁵⁰ A Fe³⁺ satellite peak was also detected at 720 eV. About 70-75% of the total iron signal corresponds to Fe(III). No significant differences were found in the global atomic ratios for the Fe peaks as a function of the scan rate.

Cr species were only found in the oxide films formed at the higher scan rates (5 and 10 mV s⁻¹), as shown in Figure 6b. The signal detected at around 577 ± 0.1 eV shows the presence of Cr³⁺ oxide compounds.⁵¹ For the layer formed at 10 mV s⁻¹, an additional peak is found at 579.9 eV, which admits two interpretations depending on the authors: non-stoichiometric CrO_x oxides as already reported⁵² or CrO₃.^{42,53,54} The performed XPS analysis does not allow to estimate the thickness of the oxide layers. However, the existence of Cr oxides only at high scan rates, generally expected to be present at the inner part of the passive layer,⁵⁰ could be related to thinner films (magnetite component), according to the electrochemical results. A more heterogeneous magnetite development for the faster scans cannot be completely excluded. The binding energies of the main peaks detected are presented in Table 3.

Table 3. Binding energies (eV) for the O 1s, Fe 2p_{3/2}, Cr 2p_{3/2} and Mo 3d signals of the films

	NaOH			NaCl	Na ₂ SO ₄
	2 mV s ⁻¹	5 mV s ⁻¹	10 mV s ⁻¹	5 mV s ⁻¹	5 mV s ⁻¹
O 1s	530.6	530.0	530.1	530.1	530.1
	532.8	532.1	532.4	532.2	532.4
	534.8	534.2	535.3	534.2	534.7
Fe 2p _{3/2}	708.5	707.8	–	708.8	708.2
	710.3	710.3	710.3	710.4	710.2
	711.6	712.0	711.6	711.9	711.7
	713.2	713.1	713.4	713.7	713.3
Cr 2p _{3/2}	–	577.1	576.9	577.1	577.4
	–	–	580.0	–	–
Mo 3d	231.5				

Effect of the electrolyte composition

In this section, the effect of the electrolyte composition in the electrochemical behavior of the oxide layer properties is discussed considering the effect of the anions OH⁻, Cl⁻ and SO₄²⁻. Oxide films were grown at a fixed 5 mV s⁻¹ scan rate in different aqueous solutions: 0.1 mol L⁻¹ NaOH (data presented in the previous section), 0.1 mol L⁻¹ NaOH + 0.1 mol L⁻¹ NaCl, 0.1 mol L⁻¹ Na₂SO₄ and 0.1 mol L⁻¹ NaCl. The potential range explored was shifted according to the pH variation.⁵⁵

Figure 7a shows a comparison of the 20th cycle (after oxide development) obtained in alkaline pH (0.1 mol L⁻¹ NaOH) with and without chloride ions. Differences are hardly visible after the contamination with chlorides, in good agreement with Addari *et al.*⁷ The characteristic

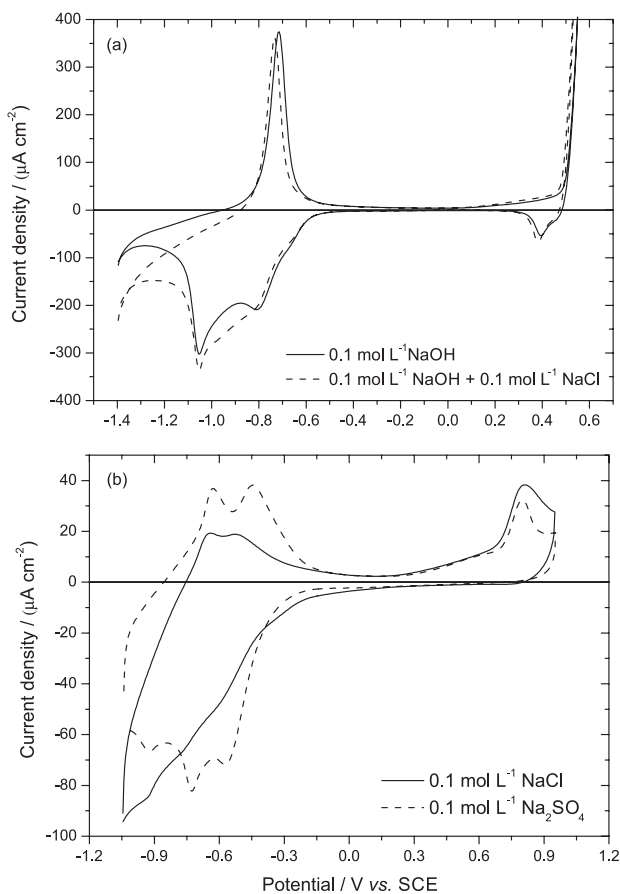


Figure 7. Cyclic voltammograms (20th cycle) obtained in the indicated alkaline (a) and neutral (b) electrolytes. The scan rate was 5 mV s⁻¹.

signals and the current density values are very close. The impedance measurements carried out before and after the cyclic polarizations (data not shown) confirmed negligible variations on the electrochemical response in the presence of this concentration of chlorides. No significant chloride incorporation into the oxide layer was previously found in agreement with other authors.⁵⁰

Figure 7b shows the curves obtained in neutral media. No major differences were found by the effect of changing the electrolyte anions. The effect of chlorides is however evident, resulting in lower anodic currents around the magnetite formation peak in NaCl solution.

There are some differences when the results are compared to the ones presented in the previous section for alkaline solutions. Firstly, the potential peaks are shifted positively, according to the pH decrease and in good agreement with the behavior expected from the Pourbaix diagram.⁵⁵ Besides, the peak assigned to the partial oxidation of magnetite, obtaining goethite as final product is, in neutral media, more evidenced.

Finally, the peaks corresponding to the redox processes of iron show significantly lower intensity (one order of magnitude less) than those measured in alkaline medium.

This decrease can be understood if the reaction for the magnetite formation is considered (equation 1). Thus, for a lower hydroxide content, due to the lower pH, the oxidation of FeO to magnetite is hindered. Therefore, as the pH decreases, the magnetite content in the passive oxide film should decrease, in agreement with previous studies.^{30,56,57}

EIS results also highlight some differences comparatively to the films grown in alkaline media. The Bode diagrams obtained before and after the polarization in the corresponding solutions at pH 7 are depicted in Figure 8. Table 2 summarizes the fitting results obtained following the equivalent circuit presented in Figure 4d.

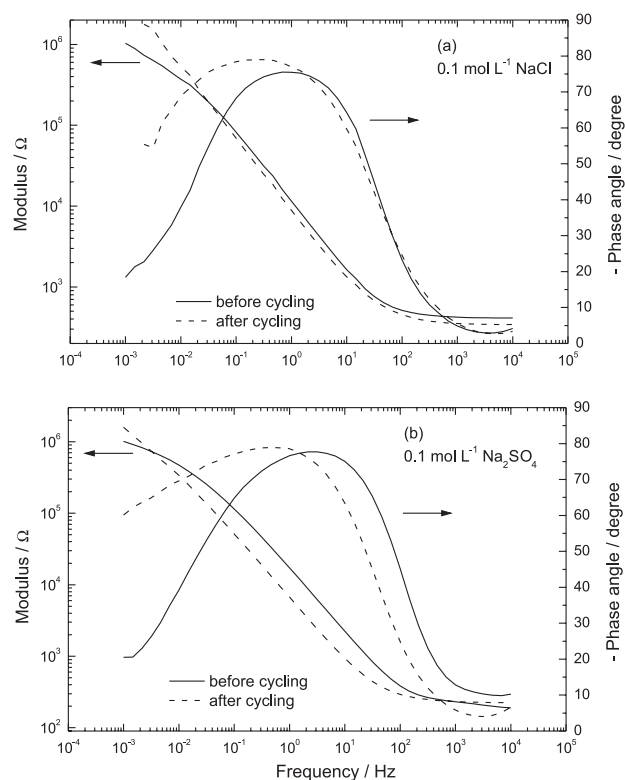


Figure 8. Bode plots measured before and after cycling at 5 mV s⁻¹ in (a) 0.1 mol L⁻¹ NaCl and (b) 0.1 mol L⁻¹ Na₂SO₄ solutions.

For the oxide films developed at neutral pH, the increase in the R₂ values is significantly higher than that observed at alkaline pH, which indicates slower magnetite oxidation process. This result is in good agreement with the lower amount of magnetite found in the polarization curves, and can be understood using equation 5: lower OH⁻ concentration hinders the oxidation process.

The redox capacitance (C₂) also increases after cycling, showing that more charge is stored in the oxide film. This variation can be associated with higher incorporation of anions (Cl⁻ or SO₄⁻²) from the electrolyte in the outer part of the film, at lower pH values. Actually, the increase in

C_2 for the oxide developed in Na_2SO_4 is more noticeable pointing out a more significant incorporation of SO_4^{2-} in the oxide layer in comparison with the Cl^- , in agreement with Mitrovic-Scepanovic *et al.*⁵⁸ However, neither Cl^- nor SO_4^{2-} were detected by XPS in the films formed under these conditions, which accounts for a low content of anions on the surface or just surface adsorption processes.²⁶

The characteristic binding energies for the O 1s and Fe 2p_{3/2} peaks are similar to those discussed in the previous section and summarized in Table 3. Thus, the three components were also distinguished for the O 1s ionization and the four components for the Fe 2p_{3/2} ionization.

No significant variation was detected in the oxide/hydroxide ratio and a slight increase was measured in the Fe^{2+} relative atomic percentage (40%) in comparison to the values obtained in alkaline conditions. The neutral pH makes the oxidation of the Fe^{2+} species (equation 1) more difficult, in agreement with that discussed above from the electrochemical results.

The Mo 3d peak is slightly better resolved at neutral pH (Figure 9). The main difference is the detection of Mo^{6+} species at 231.7 ± 0.3 eV,^{59,60} although the weak signal does not allow a concluding statement. However, this result would be in agreement with the known higher solubility of the Mo^{6+} -containing species in alkaline solutions.⁶¹ A reduced Mo fraction for higher pH value has been also measured by Liu *et al.*⁶⁰ in the acidic range.

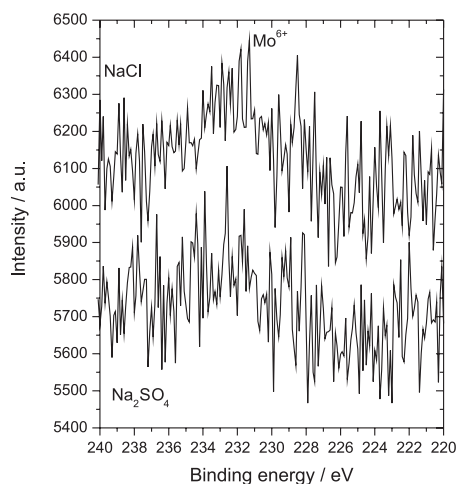


Figure 9. XPS spectra of the Mo 3d ionization for the films formed in 0.1 mol L^{-1} NaCl and 0.1 mol L^{-1} Na_2SO_4 at 5 mV s^{-1} . No signal was detected for the Mo 3d at alkaline electrolyte as discussed in the text.

Thus, alkaline pH favors the formation of magnetite on steels, in agreement with the literature,⁶¹ and Fe^{3+} oxides such as FeOOH are the main component in the films generated potentiodynamically.

The corresponding SEM pictures taken for the films formed in NaCl and Na_2SO_4 are depicted in Figure 10. In

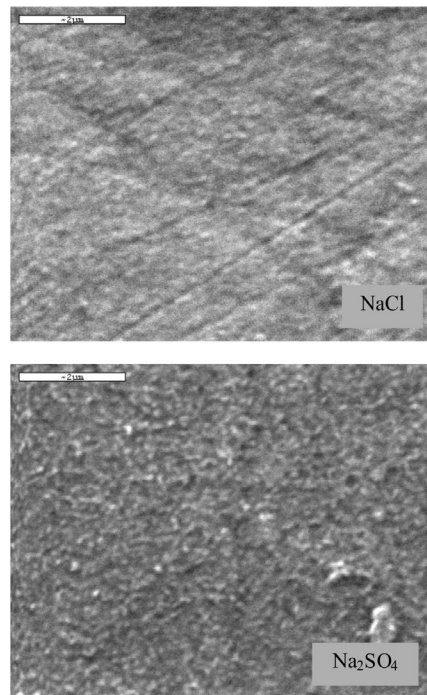


Figure 10. SEM images obtained after cycling in 0.1 mol L^{-1} NaCl and 0.1 mol L^{-1} Na_2SO_4 solutions (5 mV s^{-1}), magnification of 15000 \times .

comparison with the oxide generated in alkaline solution (at 5 mV s^{-1}), a less uniform film is formed at neutral pH, especially for the NaCl electrolyte.

The above discussed results are relevant not only for the better understanding of the oxidation phenomena but also for practical aspects related to energy storage technologies. The use of oxides on stainless steel substrates as electrodes in batteries could become an interesting strategy to minimize costs and to improve its life service. Oxide layers can be easily developed with a variety of properties by tuning the experimental parameters.

Conclusions

The present work reveals some interesting features concerning the formation and electrochemical characterization of passive films formed on the stainless steel AISI 316 in various electrolytes. The effect of changing the electrolyte conditions affects two main properties of the surface film: thickness and conductivity. This one has implications on further applications where accurate control of the resistivity is needed.

The films generated potentiodynamically become less conductive as the cycling progresses due to Fe(III) enrichment. This transformation is faster for the films developed at high scan rate. The main component for all the studied oxide layers is a Fe(III) -hydroxide compound,

probably FeOOH. The hydroxide contribution is more significant for the faster cycling rate contributing to the development of more resistive films.

In neutral media, the lower concentration of hydroxyl ions makes more difficult the transformation process of the iron oxides. In consequence, a higher percentage of Fe species with lower oxidation state were identified in the XPS study. On the other hand, the lower amount of magnetite in the films formed in neutral solutions leads to more resistive layers in comparison with alkaline electrolytes.

As demonstrated, electrochemical methods are useful tools to promote oxide films growth, while studying its electrochemistry. They provide rapid, accurate and quantitative information, concerning oxide films of metallic substrates combined with surface analysis. These results contribute to understand how these materials are affected by different ageing conditions, thus making the application of these materials more reliable in service conditions.

Acknowledgements

This work was partially supported by the Spanish “Ministerio de Economía y Competitividad” through the project BIA2010-16950. The financial support from the project PTDC/ECM/69132/2006 is also acknowledged.

References

- Olsson, C.-O. A.; Landolt, D.; *Electrochim. Acta* **2003**, *48*, 1093.
- Christensen, P. A.; Hamnett, A.; *Techniques and Mechanisms in Electrochemistry*; Blackie Academic & Professional, Chapman & Hall: Glasgow, Scotland, 1994.
- Thomas, F. G.; Henze G.; *Introduction to Voltammetric Analysis, Theory and Practice*; CSIRO Publishing: Melbourne, Australia, 2001.
- Grugeon, S.; Laruelle, S.; Dupont, L.; Chevallier, F.; Taberna, P. L.; Simon, P.; Gireaud, L.; Lascaud, S.; Vidal, E.; Yrieix, B.; Tarascon, J. M.; *Chem. Mater.* **2005**, *17*, 5041.
- Martini, M. A. M. E.; Iduvirges, L. M.; *Corros. Sci.* **2000**, *42*, 443.
- Valcarce, M. B.; Vázquez, M.; *Electrochim. Acta* **2008**, *53*, 5007.
- Addari, D.; Elsener, B.; Rossi, A.; *Electrochim. Acta* **2008**, *53*, 8078.
- Lai, W. Y.; Zhao, W. Z.; Yin, Z. F.; Zhang, J.; *Surf. Interface Anal.* **2012**, *44*, 418.
- Freire, L.; Nóvoa, X. R.; Montemor, M. F.; Carmezim, M. J.; *Mater. Chem. Phys.* **2009**, *114*, 962.
- Benzakour, J.; Derja, A.; *J. Electroanal. Chem.* **1997**, *437*, 119.
- Kocijan, A.; Donik, C.; Jenko, M.; *Corros. Sci.* **2006**, *49*, 2083.
- Veleva, L.; Alpuche-Avilés, M. A.; Graves-Brook, M. K.; Wipf, D. O.; *J. Electroanal. Chem.* **2002**, *537*, 85.
- Veleva, L.; Alpuche-Avilés, M. A.; Graves-Brook, M. K.; Wipf, D. O.; *J. Electroanal. Chem.* **2005**, *578*, 45.
- Motooka, T.; Sugie, Y.; Fujii, S.; *Corrosion* **1992**, *48*, 540.
- Sánchez, M.; Mahmoud, H.; Alonso, M. C.; *J. Solid State Electrochem.* **2012**, *16*, 1193.
- Abreu, C. M.; Cristóbal, M. J.; Losada, R.; Nóvoa, X. R.; Pena, G.; Pérez, M. C.; *Electrochim. Acta* **2006**, *51*, 1881.
- Lokhande, C. D.; Dubal, D. P.; Joo, O.-S.; *Curr. Appl. Phys.* **2011**, *11*, 255.
- Stoller, M. D.; Park, S.; Zhu, Y.; An, J.; Ruoff, R. S.; *Nanoletters* **2008**, *8*, 3498.
- Prasad, K. R.; Miura, N.; *Electrochem. Commun.* **2004**, *6*, 849.
- Demarconnay, L.; Béguin, F.; *Electrochem. Commun.* **2010**, *12*, 414.
- Daub, K.; Zhang, X.; Wang, L.; Qin, Z.; Noël, J. J.; Wren, J. C.; *Electrochim. Acta* **2011**, *56*, 6661.
- Collazo, A.; Covelo, A.; Izquierdo, M.; Nóvoa, X. R.; Pérez, C.; *Prog. Org. Coat.* **2008**, *63*, 291.
- Guzmán, R. S. S.; Vilche, J. R.; Arvía, A. J.; *Electrochim. Acta* **1979**, *24*, 395.
- Abreu, C. M.; Cristóbal, M. J.; Nóvoa, X. R.; Pena, G.; Pérez, M. C.; *Electrochim. Acta* **2002**, *47*, 2215.
- Lorang, G.; Da Cunha Belo, M.; Simoes, A. M. P.; Ferreira, M. G. S.; *J. Electrochem. Soc.* **1994**, *141*, 3347.
- Abreu, C. M.; Cristóbal, M. J.; Losada, R.; Nóvoa, X. R.; Pena, G.; Pérez, M. C.; *J. Electroanal. Chem.* **2004**, *572*, 335.
- Sánchez, M.; Gregori, J.; Alonso, C.; García-Jareño, J. J.; Takenouti, H.; Vicente, F.; *Electrochim. Acta* **2007**, *52*, 7634.
- Abreu, C. M.; Cristóbal, M. J.; Losada, R.; Nóvoa, X. R.; Pena, G.; Pérez, M. C.; *Electrochim. Acta* **2004**, *49*, 3057.
- Weast, R.; *Handbook of Chemistry and Physics*, 55th ed.; CRC Press: Cleveland, Ohio, USA, 1975, p. B-99
- Freire, L.; Carmezim, M. J.; Ferreira, M. G. S.; Montemor, M. F.; *Electrochim. Acta* **2010**, *55*, 6174.
- Abreu, C. M.; Cristóbal, M. J.; Losada, R.; Nóvoa, X. R.; Pena, G.; Pérez, M. C.; *Electrochim. Acta* **2006**, *51*, 2991.
- Bond, A. M.; *Broadening Electrochemical Horizons*; Oxford University Press Inc.: New York, USA, 2002.
- Bautista, A.; Blanco, G.; Velasco, F.; Gutiérrez, A.; Palacín, S.; Soriano, L.; Takenouti, H.; *Mater. Constr.* **2007**, *57*, 17.
- Joiret, S.; Keddad, M.; Nóvoa, X. R.; Pérez, M. C.; Rangel, C.; Takenouti, H.; *Cem. Concr. Compos.* **2002**, *24*, 7.
- Conway, B. E.; *Electrochemical Supercapacitors Scientific Fundamentals and Technological Applications*; Plenum Pub.: New York, USA, 1999.
- Andrade, C.; Merino, P.; Nóvoa, X. R.; Pérez, M. C.; Soler, L.; *Mater. Sci. Forum* **1995**, *192-194*, 891.

37. Andrade, C.; Keddani, M.; Nóvoa, X. R.; Pérez, M. C.; Rangel, C.; Takenouti H.; *Electrochim. Acta* **2001**, *46*, 3905.
38. Sánchez-Moreno, M.; Takenouti, H.; García-Jareño, J. J.; Vicente, F.; Alonso, C.; *Electrochim. Acta* **2009**, *54*, 7222.
39. Guitián, B.; Nóvoa, X. R.; Puga, B.; *Electrochim. Acta* **2011**, *56*, 7772.
40. Grosvenor, A. P.; Kobe, B. A.; McIntyre, N. S.; *Surf. Sci.* **2004**, *572*, 217.
41. Cornell, R. M.; Schwertmann, U.; *The Iron Oxides: Structure, Properties, Reactions, Occurrences and Uses*, 2nd ed.; Wiley-VCH: Weinheim, Germany, 2003.
42. MacIntyre, N. S.; Zetaruk, D. G.; *Anal. Chem.* **1977**, *49*, 1521.
43. Descostes, M.; Mercier, F.; Thromat, N.; Beaucaire, C.; Gautier-Soyer, M.; *Appl. Surf. Sci.* **2000**, *165*, 288.
44. Brion, D.; *Appl. Surf. Sci.* **1980**, *5*, 133.
45. Asami, K.; Hashimoto, K.; Shimodaira, S.; *Corros. Sci.* **1976**, *16*, 35.
46. Di Castro, V.; Ciampi, S.; *Surf. Sci.* **1995**, *331-333*, 294.
47. Asami, K.; Hashimoto, K.; *Corros. Sci.* **1977**, *17*, 559.
48. Droubay, T.; Chambers, S. A.; *Phys. Rev. B: Condens. Matter Mater. Phys.* **2001**, *64*, 2054141.
49. Grovesnor, A. P.; Kobe, B. A.; Biesinger, M. C.; McIntyre, N. S.; *Surf. Interface Anal.* **2004**, *36*, 1564.
50. Mischler, S.; Vogel, A.; Mathieu, H. J.; Landolt, D.; *Corros. Sci.* **1991**, *32*, 925.
51. Keller, P.; Strehblow, H. H.; *Corros. Sci.* **2004**, *46*, 1939.
52. Hryniewicz, T.; Rokosz, K.; Rokicki R. M.; *Corros. Sci.* **2008**, *50*, 2676.
53. Brooks, A. R.; Clayton, C. R.; Doss, K.; Lu, Y. C.; *J. Electrochem. Soc.* **1986**, *133*, 2459.
54. Clayton, C. R.; Lu, Y. C.; *J. Electrochem. Soc.* **1986**, *133*, 2465.
55. Pourbaix, M.; *Atlas of Electrochemical Equilibria in Aqueous Solutions*; Pergamon: New York, USA, 1966.
56. Freire, L.; Catarino, M. A.; Godinho, M. I.; Ferreira, M. J.; Ferreira, M. G. S.; Simoes, A. M. P.; Montemor, M. F.; *Cem. Concr. Comp.* **2012**, *34*, 1075.
57. Schmutz, P.; Landolt, D.; *Corros. Sci.* **1999**, *41*, 2143.
58. Mitrovic-Scepanovic, V.; Brigham, R. C.; *Corros. Sci.* **1987**, *27*, 545.
59. Olejford, I.; Brox, B.; Jevestam, V.; *J. Electrochem. Soc.* **1985**, *132*, 2854.
60. Liu, C. T.; Wu, J. K.; *Corros. Sci.* **2007**, *49*, 2198.
61. Bautista, A.; Blanco, G.; Velasco, F.; Gutiérrez, A.; Soriano, L.; Palomares, F. J.; Takenouti, H.; *Corros. Sci.* **2009**, *51*, 785.

Submitted: February 28, 2013

Published online: June 28, 2013